

Structure and charge transport of amorphous Cu -doped Ta_2O_5 : An *ab initio* study

Rajendra Thapa*

Department of Physics and Astronomy,
Nanoscale and Quantum Phenomena Institute (NQPI),
Ohio University, Athens, Ohio 45701, United States of America

Bishal Bhattarai†

Department of Physics,
Missouri University of Science and Technology,
Rolla, Missouri 65409, United States of America

M. N. Kozicki‡

Department of Electrical, Computer and Energy Engineering
Arizona State University, Tempe, AZ 85287, United States of America

Kashi N. Subedi§ and D. A. Drabold¶

Department of Physics and Astronomy,
Ohio University, Athens, Ohio 45701, United States of America

(Dated: March 17, 2020)

In this paper, we present *ab initio* computer models of Cu -doped amorphous Ta_2O_5 , a promising candidate for Conducting Bridge Random Access Memory (CBRAM) memory devices, and study the structural, electronic, charge transport and vibrational properties based on plane-wave density functional methods. We offer an atomistic picture of the process of phase segregation/separation between Cu and Ta_2O_5 subnetworks. Electronic calculations show that the models are conducting with extended Kohn-Sham orbitals around the Fermi level. In addition to that, we also characterize the electronic transport using the Kubo-Greenwood formula modified suitably to calculate the space-projected conductivity (SPC)¹. Our SPC calculations show that Cu clusters and under-coordinated Ta adjoining the Cu are the conduction-active parts of the network. We also report information about the dependence of the electrical conductivity on the connectivity of the Cu submatrix. Vibrational calculations for one of the models has been undertaken with an emphasis on localization and animation of representative modes.

I. INTRODUCTION

Novel non-volatile memory devices are an area of active inquiry. Research on ferroelectric random access memory (FeRAM) and magnetoresistive random access memory (MRAM) have been limited due to underlying technological and scalability problems². Meanwhile, study of non-volatile memory, based on electrically switchable resistance or resistive random access memory (ReRAM), has gained considerable interest. The first studies of such resistive switching was reported in the 1960's and was based on oxides in a metal-ion-metal (MIM) framework with formation/dissolution (SET/RESET) of filament electrochemical in nature³. Amongst ReRAM's, electrochemical metallization mechanism (ECM) or conductive bridging random access memory (CBRAM) which utilizes the electrochemical dissolution of an active electrode material such as Cu or Ag for SET/RESET mechanism has shown particular promise. In CBRAM, transition metals in their ionic state are converted to a conducting filament by applying a suitable electric field, which upon reversal, destroys the filament resulting in a resistive state. Several possible candidates for solid electrolytes have been studied elsewhere⁴⁻⁹. Amorphous tantalum pentoxide/amorphous tantalum ($a-Ta_2O_5$) has been investigated as a possible candidate for memory devices, anti-reflection coatings and optical waveguides due to its high dielectric

constant, high refractive index, chemical and thermal stability¹⁰⁻¹². Cu -doped $a-Ta_2O_5$ shows promising properties for CBRAM based memory devices.

Several experiments as well as calculations¹³⁻¹⁶ have been carried out to understand conduction mechanisms in Ta_2O_5 materials. In these studies^{13,15,16}, Ag , Cu , Pt metals were used as electrodes while in one *Xiao et. al.*¹⁴ used Cu nanowires of different diameters inserted into the low density Ta_2O_5 host to study transport and electronic properties of Ta_2O_5 as an electrolyte. These papers indicate that metal filaments are responsible for conduction. It has been reported that conduction paths in different electrolytes differ qualitatively. Metals such as Cu form clusters, leading to a conducting filament in oxides, while no such clustering is observed in chalcogenide based electrolytes¹. Since a complete investigation of Cu -doped Ta_2O_5 has not yet been reported, we provide here a thorough investigation amid growing research to test its candidacy as a possible electrolyte for CBRAM technologies.

In this paper, we investigate the structural, electronic and lattice dynamics of amorphous Cu -doped $a-Ta_2O_5$. We provide insights into structural properties and coordination statistics, electronic and vibrational properties, and visualize conduction/current paths by computing the space-projected conductivity (SPC)¹. We elucidate the atomistic mechanisms of phase segregation and track the emergence of Cu clusters as

the melt cools. The rest of paper is organized as follows. In section II, we discuss the computational methodology used to generate our models. This is followed by validation of the generated models with particular attention to the structural, electronic, vibrational, and thermal properties in section III. In Section IV we present the conclusions of our work and future research directions.

II. METHODOLOGY AND MODELS

We prepare two 210-atom models of $a-(Ta_2O_5)_{0.80}Cu_{0.20}$ cooled at different rates by utilizing melt-quenching within the *ab initio* molecular dynamics (AIMD) method. The initial density for both of the models was chosen to be that of amorphous tantalum ($\rho = 7.79 \text{ gm/cc}$), consistent with experimental^{17,18} and theoretical studies¹⁴. We have performed molecular dynamics simulations using *ab initio* plane wave code VASP¹⁹⁻²¹ with projector-augmented wave (PAW) method²² and employed the *Perdew-Burke-Ernzerhof* (PBE)²³ exchange-correlation functional. Due to the size of the unit cell, only the Γ -point is used for Brillouin zone (BZ) integrations. A plane-wave cut off of 500 eV, a time step of 3.0 fs and Nose' thermostat was used to control the temperature.

A. Model I

We fabricated a starting model of 48 *Ta*, 120 *O* and 42 *Cu* atoms with random initial positions (with no atoms closer than 2 Å) in a cubic box of side 14.14 Å. This model was then taken through a *melt quench* (MQ)²⁴ cycle. Firstly, the system was heated well above melting point to form a liquid at 6000 K and then equilibrated at 6000 K, cooled to 3000K in 18 ps, equilibrated at 3000K for 9ps and further cooled to 300K in 15 ps summing up for a total simulation time of 57 ps. The cell volume was relaxed to obtain zero pressure models. This zero-pressure relaxation produced a volume rise of 2.09% yielding an optimized density of 7.63 gm/cc.

B. Model II

Another melt and quench (MQ) model, with slower cooling rate around the melting point of Ta_2O_5 , was made. This model started with the melt of Model I cooled to 3000K and was further cooled to 300K in 24ps without any intermediate equilibration. The total simulation time was 60 ps.

After dynamical arrest, conjugate-gradient relaxation was applied until the magnitude of the force on each atom was reduced to less than 0.01 eV/Å. Zero-pressure relaxation increased the volume by 2.39% and the density was optimized to 7.61 gm/cc. A third model, cooled faster than the models discussed here, has been described in the Supplementary Material, to provide some insight into the influence of the quench rate on the network topology.

For simplicity and consistency, we follow the same "color nomenclature" for the atomic species: *Ta*, *O*, and *Cu* atoms are colored green, red, and blue respectively.

	Atom	n	$n(Ta)$	$n(O)$	$n(Cu)$
<i>Model I</i>	<i>Ta</i>	7.96	1.75	5.52	0.69
	<i>O</i>	2.44	2.21	0.00	0.23
	<i>Cu</i>	7.17	0.79	0.67	5.71
<i>Model II</i>	<i>Ta</i>	8.00	1.92	5.60	0.48
	<i>O</i>	2.45	2.24	0.00	0.21
	<i>Cu</i>	7.48	0.55	0.60	6.33

TABLE I: Average coordination number (n) and its distribution among different species. Coordination is counted only if the distance between the atoms is no more than the sum of their covalent radius within a tolerance of 0.1 Å. Covalent radii for *Ta*, *O* and *Cu* are taken as 1.70Å, 0.73Å, and 1.32Å, respectively

III. RESULTS AND DISCUSSION

A. Structural Properties

As shown in Fig.2, the radial distribution function for both models has a first peak at 1.95Å, which arises from the dominant *Ta*-*O* bonds and corresponds to the *Ta*-*O* bond length. This peak is in agreement with experiments^{17,25} for pure $a-Ta_2O_5$ and previous DFT calculations¹³ for *Cu*-doped tantalum as well which suggests that the introduction of *Cu* to the network does not significantly change the local environment around the *Ta* atoms, i.e. the dominance of *Ta*-*O* octahedra in the structure persists even after *Cu* doping. This finding is also supported by low *Cu*-*O* coordinations. Introduction of *Cu*, however, steals some *O* coordination from *Ta*, as seen in Table I, and these under-coordinated *Ta* atoms have a significant role in conduction which will be explained later.

The *Ta*-*Ta* correlations also remain unaffected by *Cu* doping but a strong peak, at 2.48Å, in the *Cu*-*Cu* correlations suggests the formation of *Cu* clusters in the system, as seen in Fig.1, which can be attributed to the ionicity of the *Ta*-*O* bonds²⁶ that drives the *Cu*-atoms to cluster. Previously, clustering of *Cu* in ionic host ($a-Al_2O_3$) has been reported¹. This strong *Cu*-*Cu* correlation suggests that *Cu*-atoms preferentially bond with themselves, consistent with the coordination statistics. In contrast, zirconia-doped tantalum shows no *Zr* clustering and, the metal atoms distribute themselves homogeneously with no metal-metal pair closer than 2.9Å¹². It is quite interesting that our calculations "naturally" produce connected *Cu* "wires" that are extended in space (considering the periodic boundary conditions), not by modeler's "installation", but as a direct and unbiased consequence of the melt-quench simulations themselves.

Two peaks are worth mentioning in the *Ta*-*Ta* correlation: the first at around 3.3Å, and the second around 3.8Å, firstly

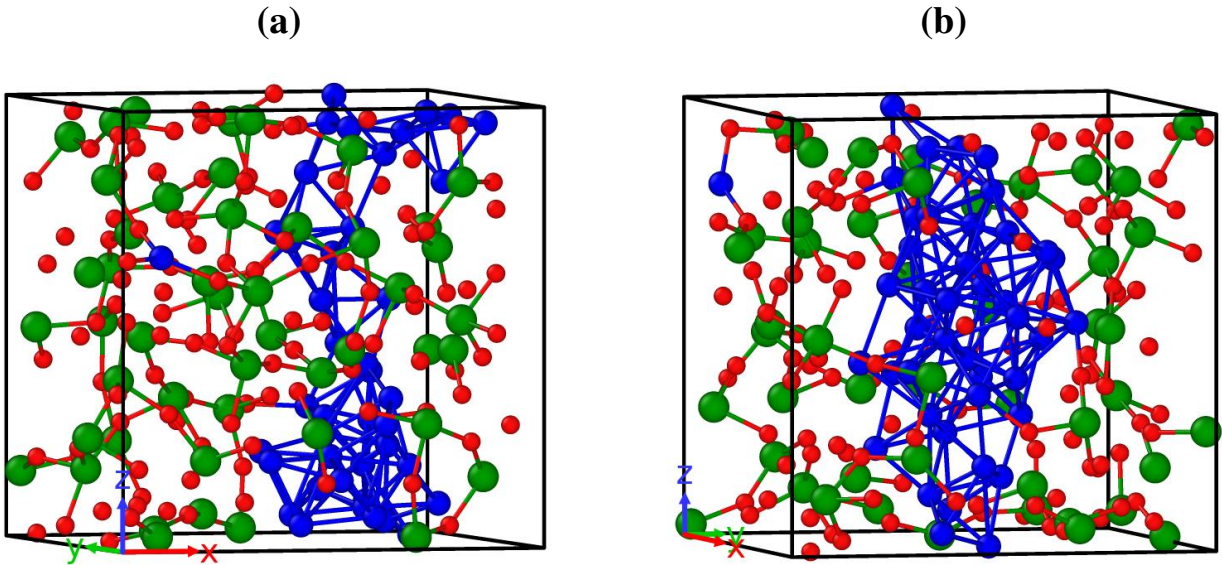


FIG. 1: (a) The structure of Model I (a) and Model II (b) consists of tantalum atoms bonded to 5, 6 and 7 oxygen atoms to form a mixture of edge-sharing, corner-sharing and face-sharing polyhedra and a connected subnetwork of *Cu* atoms. The *Cu* network grows in the interstitial space between *Ta-O* polyhedra. *Cu*, *Ta* and *O* atoms are shown in blue, green and red, respectively and the same "color nomenclature" will be used throughout the paper.

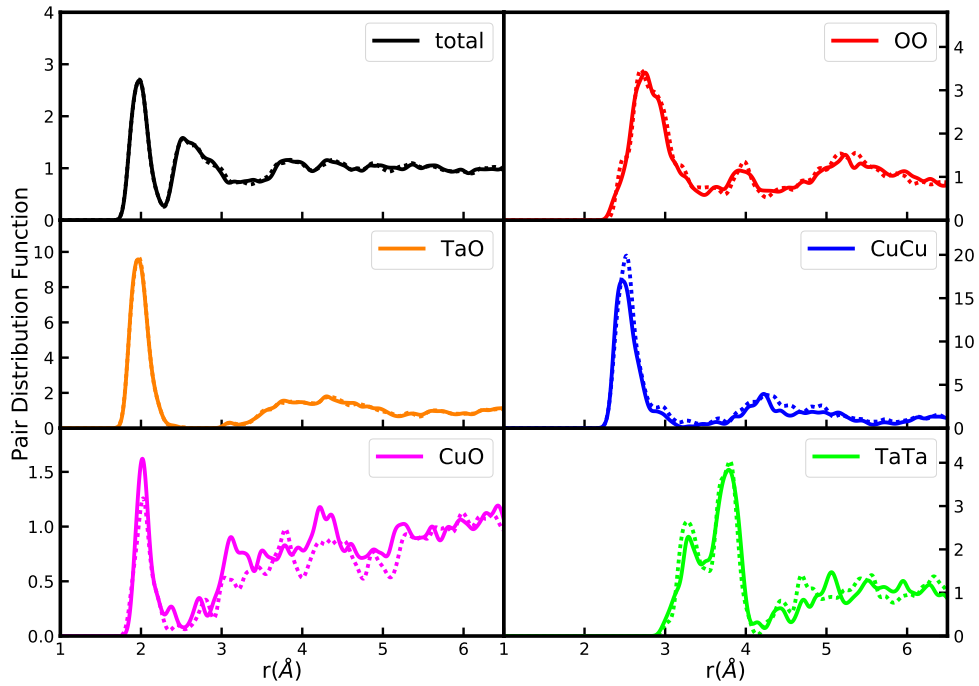


FIG. 2: Pair distribution function for Model I (solid line) and Model II (dotted line). The total pair distribution function ($g(\mathbf{r})$) is almost the same for both the models. There is, however, a slight change in the *Cu-Cu* and *Cu-O* partial correlations.

because they provide an idea of the how the *Ta-O* octahedra are connected, and secondly because they are implicated in mechanical loss for Laser Interferometer Gravity Wave Observatory application¹². The former comes from the joint contribution of face and edge-shared octahedral connection while

the latter derives from the corner-shared connection of the octahedra.

The coordination statistics of the models in Table I largely serve to validate the findings of the RDF and the correlations between different species. It also suggests that, as we lower

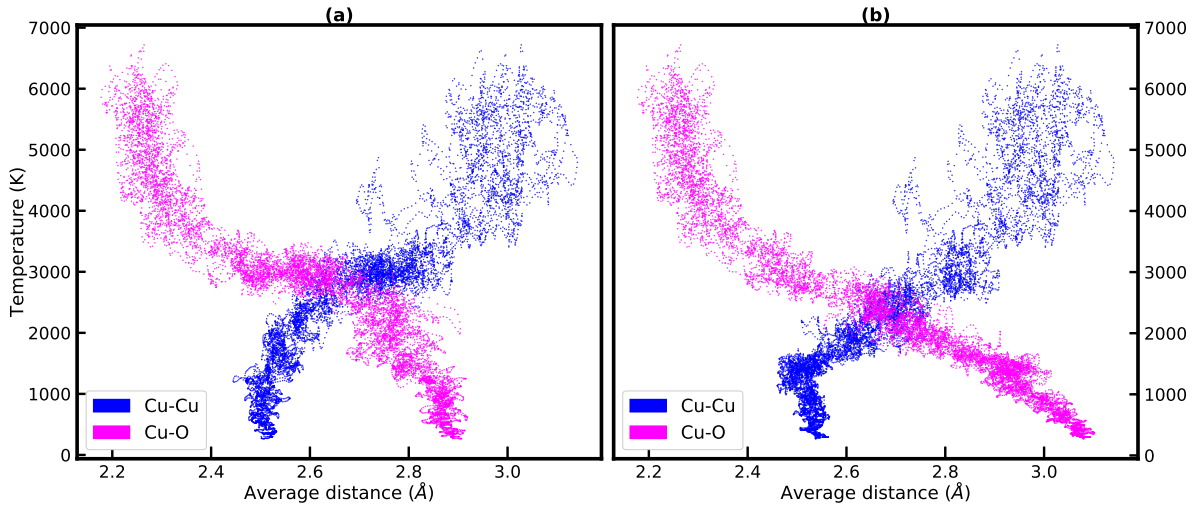


FIG. 3: Average distance of three nearest Cu to Cu atoms (blue dots) and O to Cu atoms (purple dots), averaged over all Cu atoms, for Model I (a) and Model II (b).

the cooling rate, the Cu - Cu coordination increases while the Cu - O coordination decreases. This implies slower cooling rates produce better Cu clusters with O being pushed away from them.

To compare the Cu - Cu and the Cu - O environment and its evolution during the *melt and quench* process in our models, we calculate, at each step, the following quantities:

$$d_{CuCu} = \frac{1}{3N_{Cu}} \sum_{i=1}^{N_{Cu}} \sum_{j=1}^3 |\vec{R}_{Cu,i} - \vec{R}_{Cu,j}| \quad (1)$$

$$d_{CuO} = \frac{1}{3N_{Cu}} \sum_{i=1}^{N_{Cu}} \sum_{j=1}^3 |\vec{R}_{Cu,i} - \vec{R}_{O,j}| \quad (2)$$

The sum over j runs over three nearest Cu in the first equation and over three nearest O in the second. The scatter plots in Fig. 3 show how these distances change as we cool the melt. This plot clearly shows that as we reduce the cooling rates, the O and Cu atoms move apart. Furthermore, the details of the change in the bonding environments of the atoms and the phase segregation of Cu atoms in the network during the *melt and quench* process has been discussed with animations in the Supplementary Material. There, we provide a visualization of the network formation process, and observe the exclusion of Cu as the host Ta_2O_5 network, rendering the Cu becomes *atomus non grata* in or near the Ta_2O_5 regions. The main “takeaway” from Fig. 3 is that the more extended cooling produces a more compact Cu cluster for Model II (hence the extended right “leg” on the right side of the “ballerina plot” of Fig. 3b compared to Fig 3a). This suggests that slower cooling rates create Cu clusters that are as compact as possible, and minimize Cu cluster surface area exposed to the Ta_2O_5 host. Of course this hints at a propensity to form crudely spherical clusters, though our simulations are too small to prove this assertion.

B. Electronic Properties

To understand the electronic structure of the models, we examine the total density of states (DoS), partial DoS and inverse participation ratio (IPR). These calculations not only help us check the validity of the model, but can also be used for *a priori* information to model amorphous materials^{27,28}. The plot of the DoS in Fig. 4 reveals that both models have states around the Fermi level with extended Kohn-Sham orbitals indicating conducting behavior. Since the host (Ta_2O_5) is an insulator with a band gap of $4.22eV$ ²⁹, we see that the introduction of Cu to the network closes the gap by inducing impurity bands spread throughout the *entire* host (Ta_2O_5) gap. This is corroborated by the fact that the states near the Fermi level arise from the Cu -3d orbitals hybridized mainly with Ta and small contributions from O orbitals, as seen in the partial DoS plots in Fig.4.

Our calculations show that the states near the Fermi level arise mostly due to Cu and Ta and a small contribution from O . The occurrence of Cu clusters in the Ta_2O_5 host suggest that the Cu -clusters and Ta atoms near them form the conduction-active parts. In order to study the details of the states near the Fermi level, we plot the species-projected DoS averaged over three states above and below the Fermi level in Fig.5. These plots show that states near the Fermi level arise from both Cu and Ta atoms and is shared among a fairly large number of atoms.

A further insight into the electronic properties is given by IPR defined as:

$$\mathcal{I}(\psi_n) = \frac{\sum_i |a_n^i|^4}{(\sum_i |a_n^i|^2)^2} \quad (3)$$

with a_n^i being the contribution to the eigenvector ψ_n from the i^{th} atomic orbital (s , p , and d) as obtained from VASP.

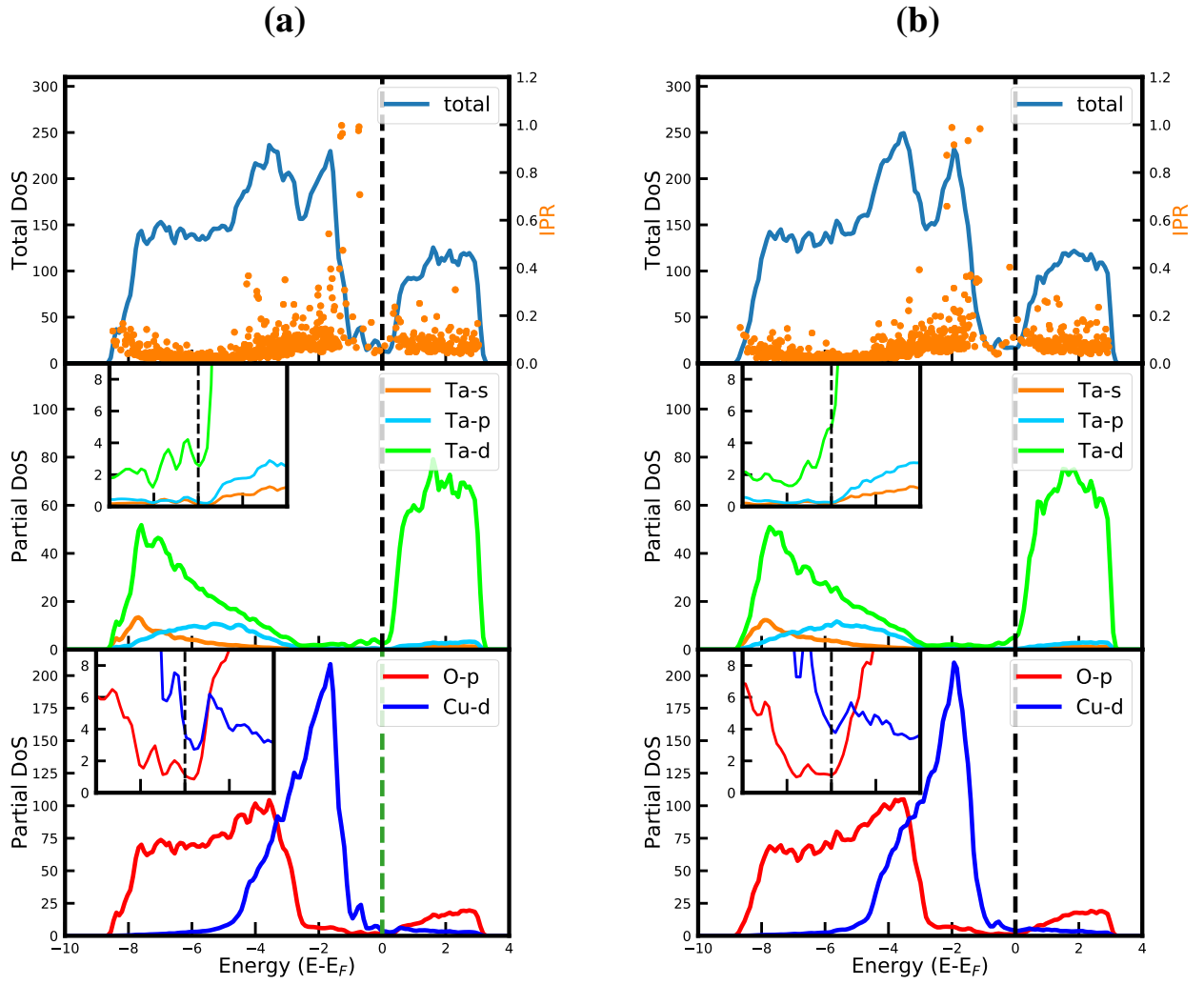


FIG. 4: Electronic density of (Kohn-Sham) states, Inverse Participation Ratio and projection onto atomic species for Model I (a) and Model II (b) with black vertical drop lines indicating Fermi level. The insets show a magnified version of the DoS contributions from each species near the Fermi Level.

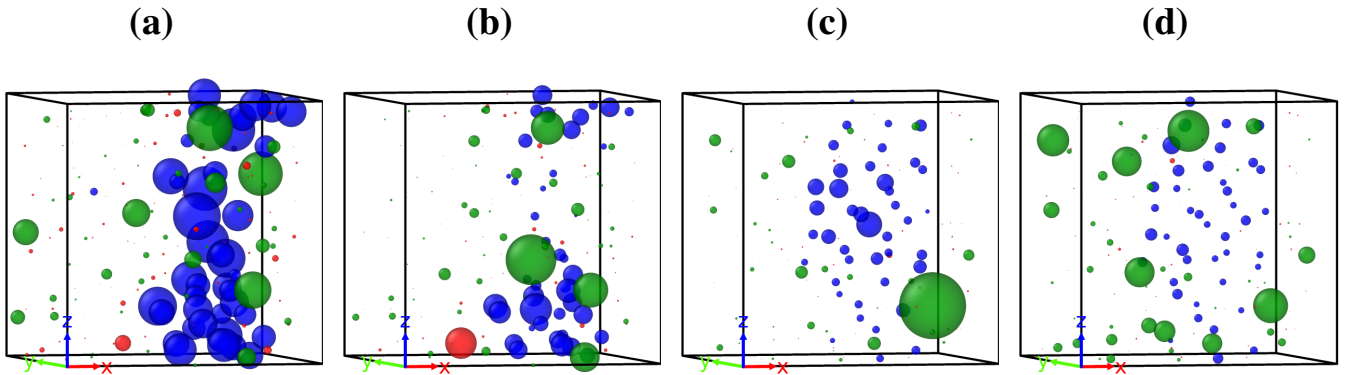


FIG. 5: Electronic DoS averaged over three bands below ((a) for Model I and (c) for Model II) and above ((b) for Model I and (d) for Model II) the Fermi level. The size of the atoms is proportional to their contribution to the total DoS. Colors as in Fig. 1.

In physical terms, IPR of electronic states is a measure of localization: localized state having high IPR value (ideally

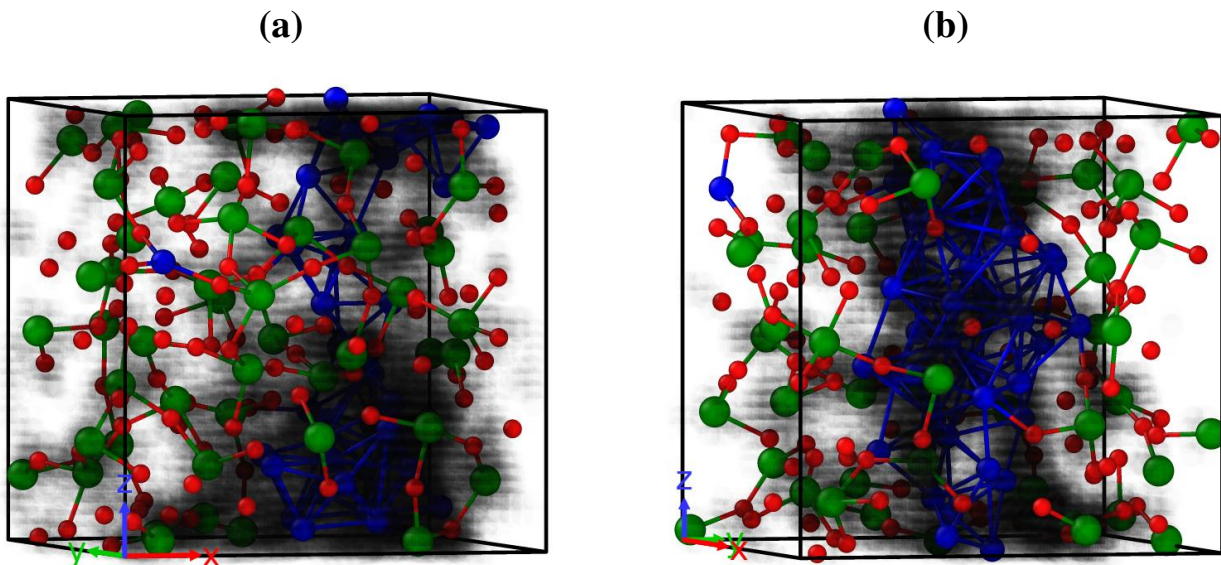


FIG. 6: Space Projected Conductivity scalar field for Model I(a) and Model II(b) shown in grayscale. Those parts of the network containing the interlinked Cu -atoms are clearly more conducting in both models. The electrical conductivity of Model II is about 5 times that of Model I, because of the more robust Cu filament of Model II.

equal to $\mathcal{I} = 1$) while a completely extended state having a value of $(1/N)$, i.e. evenly distributed over N atoms. Near the Fermi level, we observe low IPR indicating delocalized states and conducting behavior of the models.

1. Space Projected Conductivity

The density of states provides some hints about the species contributing near the Fermi-level; however, the conduction also depends upon the localization of their electronic states and momentum matrix elements between Kohn-Sham states near the Fermi level. Recently, we have developed a spatial decomposition of the Kubo-Greenwood^{30,31} formula that provides information about conducting paths in real space. By introducing a discrete grid in space, we show that the quantity:

$$\zeta(\mathbf{x}) = \left| \sum_{\mathbf{x}} \Gamma(\mathbf{x}, \mathbf{x}) \right| \quad (4)$$

provides such information at the spatial grid point \mathbf{x} and for which:

$$\Gamma(\mathbf{x}, \mathbf{x}') = \sum_{ij\alpha} g_{ij} \xi_{ij}^{\alpha}(\mathbf{x}) (\xi_{ij}^{\alpha}(\mathbf{x}'))^*. \quad (5)$$

Here, g_{ij} is defined in *Prasai et. al*¹ and $\xi_{ij}^{\alpha}(\mathbf{x}) \equiv \psi_i^*(\mathbf{x}) p^{\alpha} \psi_j(\mathbf{x})$ is a complex-valued function, $\psi_i(\mathbf{x})$ is the i^{th} Kohn-Sham eigenfunction and $p^{\alpha} = \frac{\hbar}{i} \frac{\partial}{\partial x_{\alpha}}$, ($\alpha = x, y, z$).

We have used this approach to describe transport in a solid electrolyte material¹ and Cu -doped α -alumina³². In a mixed (insulating/conducting) system like ours only a few eigenvectors of Γ characterize essentially all conduction in the system.

The SPC for both models is visualized as a grayscale plot in Fig.6. The figure shows that connected Cu atoms form primary sites of conduction as expected. However, some Ta atoms, which are near the Cu atoms also contribute significantly to the electronic conduction. A detailed analysis of the bonding environment of these Ta atoms show that they are under-coordinated with oxygen, i.e. have less than (or equal to) five O bonds, a result that is in agreement with previous works on non-stoichiometric tantalum³³. A detailed discussion of the bonding environment and the coordination statistics of these Ta atoms has been made in the Supplementary Material. Furthermore, slower cooling rates produces higher Cu - Cu coordination and better connectivity, thereby enhancing conductivity. There is a factor of about 5 higher conduction in Model II than Model I, presumably because of the small “neck” interlinking Cu in Model I.

C. Vibrational Properties

1. Vibrational Density of States

The vibrational density of states (VDOS) provides key information about local bonding environments in amorphous solids and serves as a test to validate a model³⁴. Model I was well relaxed, and the lattice vectors were simultaneously relaxed to attain zero pressure, which of course produces a slightly non-orthogonal supercell. We displaced each atom

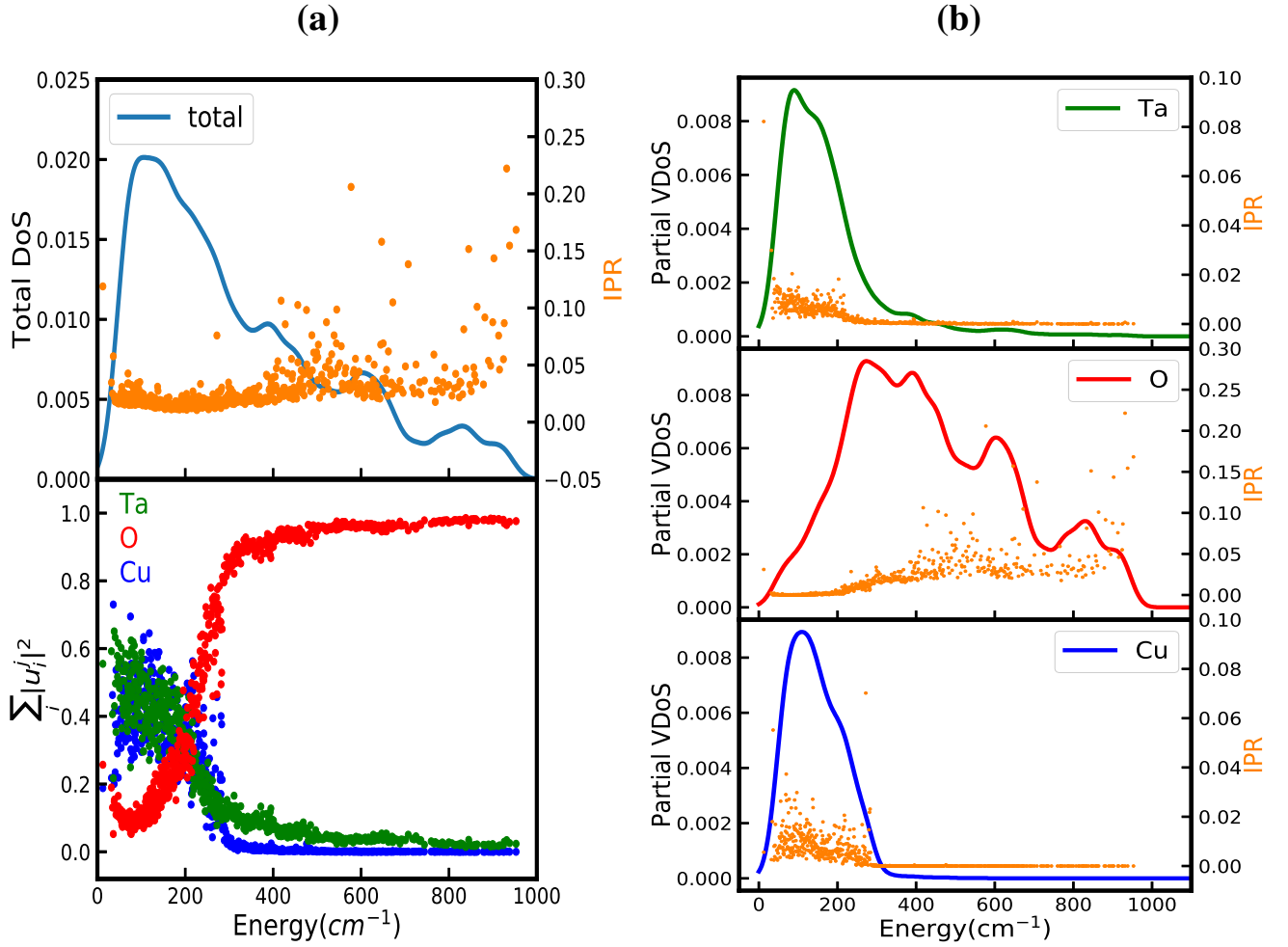


FIG. 7: **(a, top panel)** Total vibrational density of states for the *Cu*-doped Ta_2O_5 (Model I) and the magnitude of normalized eigenvectors averaged over atomic species ($|u_i^j|^2$) in **(a, bottom panel)**. A transition is seen at frequency $\sim 270\text{cm}^{-1}$ where the Oxygen atoms start dominating the vibrational spectrum. The total vibrational localization (IPR) in **(a, top panel)** shows that phonons modes are mostly extended with few localized modes appearing at higher frequencies. The yellow circles show IPR that indicates localization of vibrational eigenmodes. **(b)** We plot species-projected VDoS and VIPR of our Model I. We observe that oxygen dominates the higher frequency range and the *Cu* sub-network modes are mostly extended in nature.

in six directions ($\pm x, \pm y, \pm z$) by ($\sim 0.015 \text{ \AA}$), and after each of these small displacements, forces were computed on all atoms, to obtain the force constant matrix, and dynamical matrix³⁵. Classical normal modes were computed from the dynamical matrix by direct diagonalization. The VDOS is defined as:

$$g(\omega) = \frac{1}{3N} \sum_{i=1}^{3N} \delta(\omega - \omega_i) \quad (6)$$

, with N and ω_i representing the number of atoms and the eigenfrequencies of normal modes, respectively. To determine the elemental contribution to the VDOS, we computed species projected VDOS defined as³⁶:

$$g_\alpha(\omega) = \frac{1}{3N} \sum_{i=1}^{N_\alpha} \sum_n |e_i^n|^2 \delta(\omega - \omega_n) \quad (7)$$

, $|e_i^n|^2$ are the eigenvectors of the normal modes and N_α is total number of atoms of α species. These species-projected VDOS must satisfy the relation $g(\omega) = \sum_\alpha g_\alpha(\omega)$.

As seen in Fig.7 (left panel), the VDOS is peaked at $\sim 105\text{cm}^{-1} \approx 13\text{meV}$, a peak arising due to the mixing of vibrational motion of *Ta* and *Cu* atoms. Partial VDOS plot (right panel) shows that *Ta*- and *Cu*- vibrations are both peaked at $\sim 105\text{cm}^{-1}$ while the *O* atoms do not contribute to low frequency vibrations as significantly as the other species. However, at frequencies above $\sim 400\text{cm}^{-1}$, VDOS contributions arise mainly from the *O*-atoms, with no mixing, which can be ascribed to the low atomic mass of *O* compared to *Cu* - and *Ta* - atoms. In the intermediate region ($200\text{ cm}^{-1} - 320\text{ cm}^{-1}$), vibrations arise from combined contributions of all atomic species. Animations of selected modes are provided in the Supplementary Material. Mode mixing and cross-talk between the phase-separated regions are features of these an-

imations.

2. Localization of vibrational modes

While the VDOS is an observable that can be measured almost directly from inelastic neutron scattering experiments, the localization of these vibrations are not easily observable. To study the localization of vibrational modes in the Cu -doped Ta_2O_5 , we calculate the vibrational IPR, the vibrational analogue of the electronic IPR, from the eigenvectors as shown in Equation. 8:

$$\mathcal{V}(\omega_n) = \frac{\sum_{i=1}^N |\mathbf{u}_n^i|^4}{\left(\sum_{i=1}^N |\mathbf{u}_n^i|^2\right)^2} \quad (8)$$

where (\mathbf{u}_n^i) is displacement vector of i^{th} atom at normal mode frequency ω_n .

A small value of VIPR indicate evenly distributed vibration among the atoms while higher values imply only a few atoms contributing at that particular eigenfrequency. We have plotted the total VIPR in Fig.7. Low values of VIPR below $\sim 300 \text{ cm}^{-1}$ suggest that the vibrational modes are completely delocalized/extended. Above 300 cm^{-1} , we observe higher VIPR. To provide visual insight to the spread of vibration over atoms and localization of some vibrational modes, suitable animations and explanations of some normal modes has been provided in the Supplementary Material.

To investigate the relation between the vibrational localization and atomic species, we evaluate contribution to VIPR from each atomic species, commonly called species-projected VIPR³⁷. These projections sum up to the total VIPR, i.e. satisfy the relation:

$$\mathcal{V}(\omega_n) = \mathcal{V}_{Ta}(\omega_n) + \mathcal{V}_O(\omega_n) + \mathcal{V}_{Cu}(\omega_n) \quad (9)$$

and is shown on the right panel of Fig. 7. The species-projected VIPR calculations suggest that low frequency modes arise mainly from Ta - and Cu -atoms while the high frequency vibrations come mostly from the O -atoms which can be attributed to the atomic masses of the species. Higher

values of partial VIPR are seen at higher frequencies. Therefore, the high frequency modes are localized on a few O atoms in the network while the low frequency modes are spread among larger number of Ta and Cu atoms. The quantity plotted in the bottom left panel Fig. 7 is the squared-magnitude of normalized eigenvectors summed across the atomic species for all the normal modes. The scatter plot and the partial VDOS plots suggest that the Ta - and Cu -atoms participate almost equally in the low frequency vibrations.

IV. CONCLUSIONS

We describe the atomistic process of phase segregation of Cu in $a-Ta_2O_5$. The Cu did not significantly alter the Ta - O bonding but instead phase separated, forming Cu clusters. Models made with a slower cooling rate revealed significantly better (denser) clustering than the one with faster cooling rate. These clusters, along with the neighboring under-coordinated Ta atoms, form a conducting path in the network which is in agreement with previous literature, though presented in novel way in this paper, and not relying only on the Kohn-Sham states near the Fermi level, but also the momentum matrix elements, a legacy of the current-current correlation functions of Kubo. All this lends significant insight into an important CBRAM material.

It is interesting to speculate on what would happen in larger models and different cooling rates. We might expect to see Cu blobs in the network, possibly spatially separated but potentially interconnected by some other conducting fabric, perhaps Cu nanowires (of essential interest of course for CBRAM applications). While direct simulations like this one is computationally impossible for so large a system, it provides potentially useful *a priori* information for modeling employing simpler interatomic interactions. Electronic DoS calculations show that Cu -doping closes the gap in the DoS of pure $a-Ta_2O_5$ with extended Kohn-Sham orbitals around the Fermi level. Vibrational modes at low frequencies are shared among many Ta and Cu atoms while those at high frequency are quite localized and come only from O atoms.

V. ACKNOWLEDGEMENTS

We thank the National Science Foundation for support under grant DMR-1507670. We thank Dr. Kiran Prasai of Stanford University for helpful discussions.

* rt887917@ohio.edu

† bb6fq@mst.edu

‡ michael.kozicki@asu.edu

§ ks173214@ohio.edu

¶ drabold@ohio.edu

¹ K. Prasai, K. N. Subedi, K. Ferris, P. Biswas, and D. A. Drabold, *physica status solidi (RRL) Rapid Research Letters* **12**, 1800238 (2018),

<https://onlinelibrary.wiley.com/doi/pdf/10.1002/pssr.201800238>.

² I. Valov, R. Waser, J. R. Jameson, and M. N. Kozicki, *Nanotechnology* **22**, 254003 (2011).

³ G. Dearnaley, A. M. Stoneham, and D. V. Morgan, *Reports on Progress in Physics* **33**, 1129 (1970).

⁴ D. Lee, S. Oukassi, G. Molas, C. Carabasse, R. Salot, and L. Perniola, *IEEE Journal of the Electron Devices Society* **5**, 283 (2017).

- ⁵ W. Chen, S. Tappertzhofen, H. J. Barnaby, and M. N. Kozicki, *Journal of Electroceramics* **39**, 109 (2017).
- ⁶ T. Tsuruoka, K. Terabe, T. Hasegawa, and M. Aono, *Nanotechnology* **21**, 425205 (2010).
- ⁷ T. Gu, T. Tada, and S. Watanabe, *ACS Nano* **4**, 6477 (2010), PMID: 20932047.
- ⁸ X. Xu, J. Liu, and M. P. Anantram, *Journal of Applied Physics* **116**, 163701 (2014).
- ⁹ S. C. Pandey, R. Meade, and G. S. Sandhu, *Journal of Applied Physics* **117**, 054504 (2015).
- ¹⁰ K. Chen, M. Nielsen, G. R. Yang, E. J. Rymaszewski, and T.-M. Lu, *Journal of Electronic Materials* **26**, 397 (1997).
- ¹¹ S. Reid and I. W. Martin, *Coatings* **6** (2016), 10.3390/coatings6040061.
- ¹² K. Prasai et. al., *Phys. Rev. Lett.* **123**, 045501 (2019).
- ¹³ T. gu, Z. Wang, T. Tada, and S. Watanabe, *Journal of Applied Physics* **106**, 103713 (2009).
- ¹⁴ B. Xiao, T. gu, T. Tada, and S. Watanabe, *Journal of Applied Physics* **115**, 034503 (2014).
- ¹⁵ N. Banno, T. Sakamoto, N. Iguchi, M. Matsumoto, H. Imai, T. Ichihashi, S. Fujieda, K. Tanaka, S. Watanabe, S. Yamaguchi, T. Hasegawa, and M. Aono, *Applied Physics Letters* **97**, 113507 (2010), <https://doi.org/10.1063/1.3488830>.
- ¹⁶ T. Tsuruoka, I. Valov, S. Tappertzhofen, J. van den Hurk, T. Hasegawa, R. Waser, and M. Aono, *Advanced Functional Materials* **25**, 6374 (2015), <https://onlinelibrary.wiley.com/doi/pdf/10.1002/adfm.201500853>.
- ¹⁷ R. Bassiri, K. B. Borisenko, D. J. H. Cockayne, J. Hough, I. MacLaren, and S. Rowan, *Applied Physics Letters* **98**, 031904 (2011), <https://doi.org/10.1063/1.3535982>.
- ¹⁸ O. L. G. Alderman, C. J. Benmore, J. Neufeind, E. Coillet, A. Mermet, V. Martinez, A. Tamalonis, and R. Weber, *Phys. Rev. Materials* **2**, 043602 (2018).
- ¹⁹ G. Kresse and J. Furthmuller, *Phys. Rev. B* **54**, 11169 (1996).
- ²⁰ M. Hacene, A. Anciaux-Sedrakian, X. Rozanska, D. Klahr, T. Guignon, and P. Fleurat-Lessard, *Journal of Computational Chemistry* **33**, 2581, <https://onlinelibrary.wiley.com/doi/pdf/10.1002/jcc.23096>.
- ²¹ M. Hutchinson and M. Widom, *Computer Physics Communications* **183**, 1422 (2012).
- ²² G. Kresse and D. Joubert, *Phys. Rev. B* **59**, 1758 (1999).
- ²³ J. P. Perdew, K. Burke, and M. Ernzerhof, *Phys. Rev. Lett.* **77**, 3865 (1996).
- ²⁴ D. A. Drabold, *The European Physical Journal B* **68(1)** (2009).
- ²⁵ B. Shyam, K. Stone, R. Bassiri, M. Fejer, M. Toney, and A. Mehta, *Scientific Reports* **6**, 32170 (2016).
- ²⁶ N. Kim and J. F. Stebbins, *Chemistry of Materials* **23**, 3460 (2011), <https://doi.org/10.1021/cm200630m>.
- ²⁷ K. Prasai, P. Biswas, and D. A. Drabold, *Phys. Status Solidi A* **213**, 1653 (2016).
- ²⁸ J. H. Los and T. D. Kühne, *Phys. Rev. B* **87**, 214202 (2013).
- ²⁹ X. Wu, S. Soss, E. Rymaszewski, and T.-M. Lu, *Materials Chemistry and Physics* **38**, 297 (1994).
- ³⁰ R. Kubo, *J. Phys. Soc. Jpn.* **12**, 570 (1957).
- ³¹ D. A. Greenwood, *Proceedings of the Physical Society* **71**, 585 (1958).
- ³² K. N. Subedi, K. Prasai, M. N. Kozicki, and D. A. Drabold, *Phys. Rev. Materials* **3**, 065605 (2019).
- ³³ R. J. Bondi, M. P. Desjarlais, A. P. Thompson, G. L. Brennecke, and M. J. Marinella, *Journal of Applied Physics* **114**, 203 (2013).
- ³⁴ G. P. Lopinski, V. I. Merkulov, and J. S. Lanin, *Appl. Phys. Lett.* **69**, 3348 (1996).
- ³⁵ B. Bhattarai and D. A. Drabold, *Carbon* **115**, 532 (2017).
- ³⁶ A. Pasquarello, J. Sarnthein, and R. Car, *Phys.Rev.B* **57**, 22 (1998).
- ³⁷ B. Bhattarai, R. Thapa, and D. A. Drabold, *Modelling and Simulation in Materials Science and Engineering* **27**, 075002 (2019).